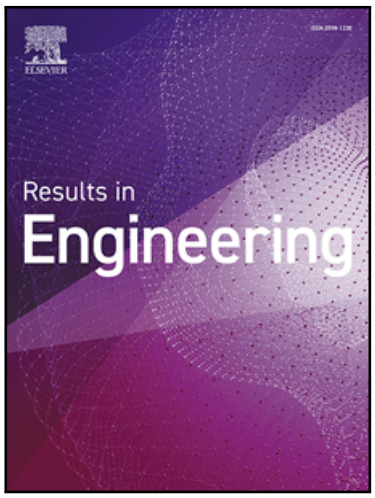

Pore Resolved Simulations of Joule Heating in Fibrous Media using an Embedded Boundary Method

Samuel Fagbemi , Vimal Ramanuj , Mohammed H. Saffarini , Philip C. Roth , Ramanan Sankaran

PII: S2590-1230(25)01847-X
DOI: https://doi.org/10.1016/j.rineng.2025.105776
Reference: RINENG 105776

To appear in: *Results in Engineering*

Received date: 29 April 2025
Revised date: 30 May 2025
Accepted date: 12 June 2025

Please cite this article as: Samuel Fagbemi , Vimal Ramanuj , Mohammed H. Saffarini , Philip C. Roth , Ramanan Sankaran , Pore Resolved Simulations of Joule Heating in Fibrous Media using an Embedded Boundary Method, *Results in Engineering* (2025), doi: https://doi.org/10.1016/j.rineng.2025.105776

Highlights:

- Electro-thermal model for studying Joule heating at the pore scale was developed
- Convective and radiative losses were modeled using an embedded boundary technique
- Rates exceeding $8x10^4$ K/s were obtained which depended on material microstructure
- Anisotropy & fiber diam. were the most dominant factors affecting peak temperature
- Coupled model provides computational framework for studying alkane dehydrogenation

Pore Resolved Simulations of Joule Heating in Fibrous Media using an Embedded Boundary Method

Samuel Fagbemi[1], Vimal Ramanuj[1], Mohammed H. Saffarini[1], Philip C. Roth[2], Ramanan Sankaran[1]

[1]Multiscale Materials Group, Oak Ridge National Laboratory
[2]Algorithms and Performance Analysis Group, Oak Ridge National Laboratory

Abstract

Joule heating has been regarded as an energy-efficient and sustainable method for heating materials and gases at large scales. The modeling of local temperature effects at pore-resolved scales for such systems, however, has been difficult to achieve due to challenges in coupling thermo-chemical processes in complex porous media and in large representative volume elements (RVEs). To this end, we developed an electro-thermal model at the pore scale to study Joule heating effects in large heterogeneous systems with different microstructures. This was achieved using the level set method to implicitly delineate distinct regions within the domain, and an embedded boundary method to facilitate heat exchange across the fluid-solid interface. Moreover, we applied this method to investigate unsteady non-linear electro-thermal effects in non-woven fibrous graphite conductors for RVEs with characteristic lengths of 2 mm, with different fiber orientations, porosity (80% – 90%) and fiber diameters (10 – 20 μm). The coupled equations were solved numerically and they produced peak temperatures greater than 2000 K resulting in heating rates as high as 80,000 K/s. Moreover, the results depended strongly on the microstructure of the fiber skeleton and current density. Geometries with large fibers (~ 20 μm) had the highest average and peak temperatures with the mean temperature increasing by 3.9 % while the peak temperature increased by 9.9 %. Anisotropic domains on the other hand had the lowest mean and peak temperatures with peak and mean temperatures of 2293 K and 1437.7K respectively representing a corresponding 12.1% and 5.1% drop in the temperatures. An increase in porosity from 80% to 90%, however, led to an increase in the peak temperature by 5.1%.

Keywords: Joule heating, flash Joule heating, pulsed heating, pore scale modeling, level set method, dehydrogenation, graphite conductors.

* Corresponding author: fagbemisa@ornl.gov

Nomenclature

L_f	Length of fiber, m	$\varphi_{min}, \varphi_{max}$	Min. and max. electrostatic potential, V
E	Electric field, Vm^{-1}	ρ	Electrical resistivity, Ωm
k_s	Thermal conductivity of fibers, $Wm^{-1}K^{-1}$	ρ_s	Density of the fibers, kgm^{-3}
c_{ps}	specific heat of fibers at constant pressure, kJ/kg/K	ψ	Level set function
T	Temperature, K	ε	Emissivity
T_{inf}	Ambient temperature. K	σ_r	Stefan-Boltzmann's constant, $Wm^{-2}K^{-4}$
Q_h	Joule heating volumetric source term, W/m^3	Ω_s	Solid domain
q_c	Convective heat loss, W/m^2	Ω_f	Fluid domain
q_r	Radiative heat loss, W/m^2	θ	Polar angle, ^{o}
q	Total heat flux, W/m^2	ϑ	Azimuthal angle, ^{o}
h	Convective heat transfer coefficient, $Wm^{-2}K^{-1}$	$\zeta_\theta, \zeta_\vartheta$	auxiliary variables of θ and ϑ
t_p	Pulse time/width, s	β	Anisotropic factor
J	Current density, A/m^2	ϕ	Porosity
n	Normal vector	Γ	Interface
$\dot{Q}_{yo}$	Weighted normalized Joule heating parameter		**Subscripts and Superscripts**
L_y	Domain length in the *y* direction, m	vD	Potential Dirichlet condition
$\hat{J}_y$	Current density in *y* direction, A/m^2	vN	Potential Neumann condition
x, y, z	Spatial coordinates, m	TD	Temperature Dirichlet condition
p_z	Fiber probability distribution in *z* plane	TN	Temperature Neumann condition
p_{xy}	Fiber probability distribution in *x-y* plane	*s, f*	Solid, fluid
nx, ny, nz	Number of grid points in *x, y* and *z* directions	*i*	Index across x plane.
PHQ	Pulsed Heating and Quenching	*j*	Index across y plane.
(F)JH	(Flash) Joule Heating	*k*	Index across z plane.
	Greek Symbols		
σ	Electrical conductivity, Sm^{-1}		
φ	Electrostatic potential, V		
φ_0	Prescribed electrostatic potential, V		

1.0 Introduction

Heating by electrification is becoming an increasingly popular heating technique due to its ability to generate large amounts of energy efficiently in a sustainable manner. In particular, Joule heating has been applied for this purpose. Joule heating or resistive heating is a process that occurs when an electrical potential gradient is created across a conductor material resulting in heat generation. Such effects may or may not be desirable depending on the application. For the latter, Joule heating due to electrokinetic flow can induce temperature gradients resulting in non-uniform material properties [1], [2], [3], [4]. Additionally, large electrical potential gradients from Joule heating can lead to material deformation and damage to circuitry. On the other hand, the Joule heating can be channeled positively for domestic and commercial uses. Domestically, it can be used for improving heat storage in phase change materials [5], for industrial applications as an alternative renewable heating source [6] and it can be applied in material design for self-reparation of composites by self-post-curing treatment of reinforced materials [7]. Additionally, it can be used to enhance and prepare materials such as graphene, and graphene oxide fibers for energy storage as well as improve their production efficiency and enhance large-scale commercialization of the materials [8].

Joule heating is also a programable electrification technique meaning that the amount of heat supplied through the introduction of electric charges can be precisely regulated and adjusted with respect to time via electric signals. This process can be applied to achieve *Flash Joule Heating (FJH)* which is a process whereby heating can be applied in certain targeted pulsed steps resulting in cycles of high temperature peaks (as high as 3000 K) and low temperature troughs. This type of technique can generate high temperatures at small time scales. Research has shown that this heating mechanism can lead to improved yields and throughputs, and is thus, cheaper than continuous heating. Dong et al. [9] applied programmable pulsed heating and quenching (PHQ) for methane dehydrogenation at pulse durations of 0.1 s resulting in peak temperatures greater than 2000 K within this timeframe while also delivering a higher conversion and selectivity of alkenes. This shows the potential of this technique for catalysis at the industrial scale. PHQ technique has also been applied in bio-systems for, cryopreservation [10] achieving high warming rates of 6×10^{8} °C/min. It has also been applied for electroporation/electro-permeabilization [11], [12], [13] and for heating nanowires [14]. The development of an efficient routine and optimal parameters computationally is crucial to the success of this method to deliver peak temperatures and yield of desired products thereby reducing design and production costs. Thus, in this work, we present an electro-thermal computational model to study PHQ Joule heating process in fibrous/porous media. Such a model would be used to simulate Joule heating when electric current is introduced at short pulses into the conductor resulting in efficient heating.

To adequately describe the Joule heating process in a heterogeneous system, it is essential to explicitly model the electric field distribution across the solid matrix to account for microstructural effects on the peak and average temperatures as opposed to the effective medium approach that uses macroscale closure terms. We thus apply the pore scale modeling approach where a static level set was used to capture the pore level information within the porous medium enabling the distinction between the regions and their respective interfaces for the multiregional system. The computational domain was discretized using a structured grid coupled with the embedded boundary method to appropriately resolve the matrix and pore spaces. This enables us to analyze large complex fiber-resolved geometries with computational efficiency. Embedded boundary methods have been mostly used for flow problems but have been applied for heat transfer-related problems in the past decades, such as works by Claassen et al. [15], Zaidi [16], Singh and Kumar [17] etc. The ability of the embedded boundary method to be carried out on stationary boundary non-conforming cartesian grid makes it an attractive choice for modeling problems with topologically complex boundaries [18]. It also does not require remeshing for problems involving moving boundaries. Thus, in this work, the ghost fluid method [19], a type of embedded boundary technique, was implemented alongside the level set method to compute the heat loss along the non-woven packed fibers. Moreover, FJH modeling was applied within the embedded boundary method framework and used to examine the effect of microstructural heterogeneity on local temperature distribution and peak temperature within the domain. The model accounts for temperature-dependent thermal properties enabling us to gain valuable scientific insights into the complex multi-physics phenomena and dependence on structural features of the reactor at the pore scale. The primary focus of our analyses is thus to investigate the effects of structural features on the Joule heating characteristics, namely, the current density, average, and peak temperatures at the pore scale. Statistical distributions of the fibrous geometry characterized in terms of its porosity, fiber diameter, and orientation are also obtained which we correlate to the electrical and temperature results. The evolution of the temperature in time during the heating phase of a single pulsed heating cycle is also examined.

This paper is arranged as follows: we present the level set model for pore scale geometry representation followed by the physical model describing the Joule heating process. We then describe how the non-woven fiber geometries were generated and implemented within the level set framework. This is followed by a discussion of the results from the study of the effect of microstructural heterogeneity on pulsed heating. The results are also compared with a theoretical model which provides an upper limit for peak temperatures for ideal conditions.

2.0 Methodology

In this section, we describe the key elements of the computational modeling approach adopted in this work. In brief, the energy conservation equation is solved using a finite difference modeling approach by resolving the fibrous skeleton. The source term arising from Joule heating effect is closed by solving the potential field distribution within the interconnected fibers. An embedded boundary formulation based on the level set function is used to capture the interfacial effects and boundary conditions on the fiber surfaces. Details of the computational geometry representation, physical model and problem setup are presented below.

2.1. Computational Model

2.1.1 Level set Equation

We begin with an outline of the level set function used to represent fibrous media at the pore scale. The classical level set (LS) method was developed by Osher and Sethain [20] for interface tracking in multiphase systems. We applied the LS distance function in this work for defining regions pertaining to the fiber skeleton and fluid. The signed distance from the interface can be expressed as:

$$|\psi(\mathbf{x})| = |\mathbf{x} - \mathbf{x}_\Gamma| \tag{1}$$

where, $\psi(\mathbf{x})$ is the level set function, which represents the signed distance from the fluid-solid interface. $\mathbf{x}_\Gamma$ is the nearest point on the interface from $\mathbf{x}$. From this definition, sub-regions can be defined implicitly based on the sign of $\psi(\mathbf{x})$. In our case solid, fluid, and interface regions can be represented by:

$$\begin{cases} \psi(\mathbf{x}) > 0, & \mathbf{x} \in \Omega_s, \quad \text{Solid}, \\ \psi(\mathbf{x}) = 0, & \mathbf{x} \in \Gamma, \quad \text{Interface}, \\ \psi(\mathbf{x}) < 0, & \mathbf{x} \in \Omega_f, \quad \text{Fluid} \end{cases} \tag{2}$$

The positive value here represents the fiber skeleton region and the negative sign for the fluid region. Figure 1 illustrates a schematic for the function distribution. A global level set value was obtained by a simple reduction i.e., taking the maximum among all fibers.

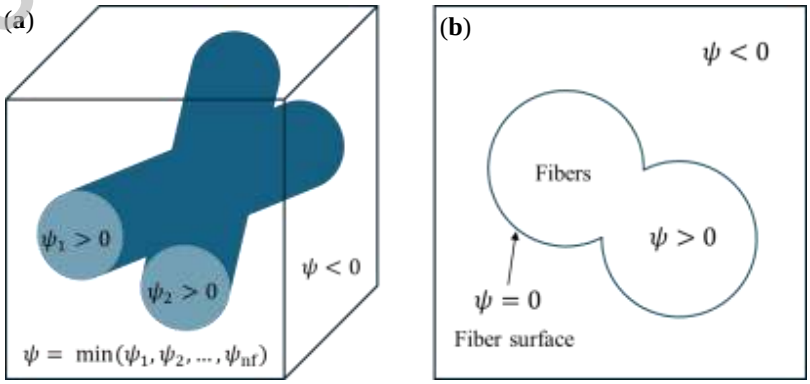

Figure 1: (a) Distribution of level set function to capture multiple fibers in a 3D domain. (b) Level set information

of 2D cross-section to implicitly capture fiber surface given by the zero isocontour. N.B. interference among fibers is intentionally retained and expected to enable current and heat transport.

In addition to capturing the fiber geometry, the distance property of the level set function is leveraged to impose the necessary embedded boundary conditions on the fiber surfaces. As will be discussed later, solving for the potential and temperature fields within the fibers involves prescribing flux conditions at the $\psi(\mathbf{x}) = 0$ surface while the governing equations are solved on the underlying grid.

2.1.2 Embedded Boundary Formulation (EBM)

The embedded boundary method is a type of a discrete forcing immersed boundary method used for modeling multi-region/multiphysics problems. Unlike the continuous forcing boundary method originally developed by Peskin [21], the discrete method does not require a localized source term for coupling physical parameters between fluid and solid domains, but rather allows for the reconstruction of the solution near the boundary after the governing equations have been discretized. The discrete forcing EBM approach also allows for a sharp delineation of the embedded boundary [22], [23]. In this implementation, stencils may cross an embedded surface and field variables on grid points outside the fibers that are not defined. In Figure 2b, for instance, one point lies inside the solid region while the other three are in the fluid region (FP). To assess the boundary values at the embedded boundary (EB), the field variables are reconstructed to have points virtually positioned at EB. The key steps involved in this method include: projecting the field values from the grid onto the interface using a prescribed surface gradient f.

$$\nabla\Theta_P = f(\psi_{I\to P}) \tag{3a}$$

$$\Theta_P = \Theta_I - \nabla\Theta_P \,.\, \psi_{I\to P} \tag{3b}$$

where Θ is any physical variable like temperature, $\psi_{I\to P}$ is the level set distance function from point I to P. The projected values of Equation (3) and are then interpolated along the interface. A quadratic or trilinear polynomial function can be applied for extrapolating the field values [17]. For sharp geometric interfaces, we applied the inverse distance weighting (IDW) [24] for reconstructing the boundary conditions at the immersed grid point nodes by the following expressions:

$$\Theta_{P*} = \frac{\sum_{i=1}^{n} w_i \Theta_i}{\sum_{i=1}^{n} w_i}, \tag{4}$$

$$\nabla\Theta_{P*} = \frac{\sum_{i=1}^{n} w_i \nabla\Theta_i}{\sum_{i=1}^{n} w_i}, \tag{5}$$

where $w_i = 1/|\,\psi_i(\mathbf{x})|$. These interpolated values depends on the weights computed at the neighboring nodes from $i = 1$ to n. Weights w_i depend primarily on the geometry of the interface and the values are

chosen such that it is maximum for projection points closest to P^* [23]. After interpolation, P^* is projected to the ghost point (GL). The ghost surface values at the ghost surface node Θ_{GL} are given as:

$$\Theta_{GL} = \Theta_{P*} + \nabla\Theta_{P^*} . \psi_{P^*\rightarrow GL} \quad (6)$$

where $\psi_{P^*\rightarrow GL}$ is the distance function from the interface to the ghost layer and the surface. Θ_{P*} is known at the surface and the gradient is computed using Equation 5. The Neumann condition Θ_{GL} on the other hand is computed using surface values Θ_{P^*} and the gradient $\nabla\Theta_{P^*}$ *via* a truncated Taylor series expansion as shown in Equation 6. This operation allows for standard difference operations (i.e., upwind, central difference, etc.) to be applied without modifications of the governing equations to incorporate embedded boundary information. This EBM implementation is second-order accurate and has an L_∞ error norm that decreases with grid refinement [24]. Moreover, validations of this method and mesh dependent studies for transfer heat applications have been shown in Ramanuj et al., [23]. And thus, we expand on it for Joule heating in this work.

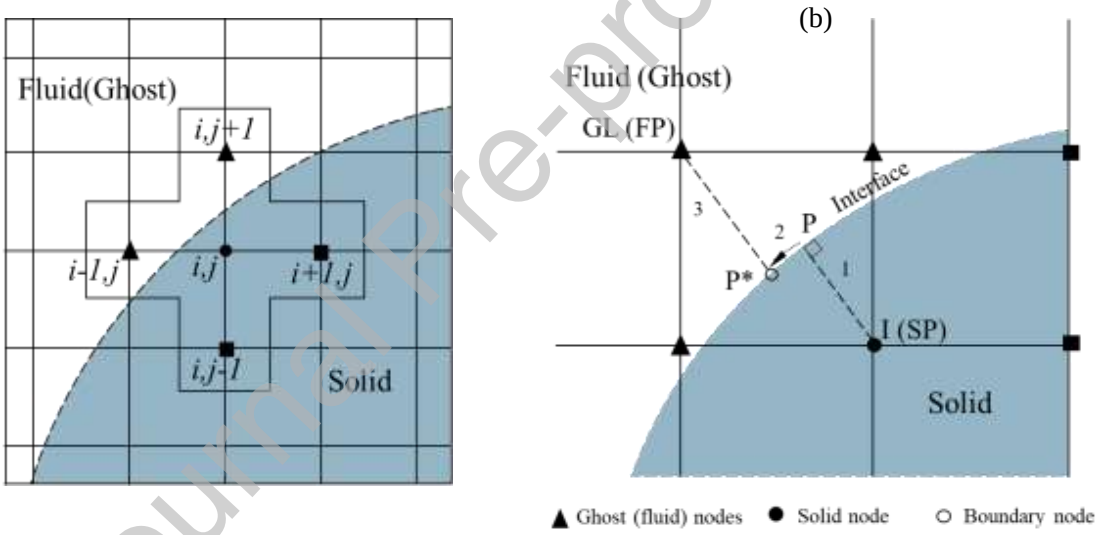

Figure 2: (a) Schematic of an embedded boundary method to capture interfacial boundary condition using level set function on a cartesian grid with a 2D central difference stencil (b) Projection of points across the boundary involving extrapolation.

2.2 Joule Heating Model

2.2.1 Electro-Thermal Model - Governing Equations

Joule or resistive heating is a heating process that occurs when electric current is passed through a conductor. The process involves the conversion of electrical to thermal energy which is dependent on the material's electric and thermal properties. The electric field **E** generated when a potential difference is applied across the ends of a conductor can be modeled by the following steady-state equation:

$$\nabla \cdot (\sigma \mathbf{E}) = 0, \tag{7}$$

where σ is the electric conductivity. Equation (7) solves for the electrostatic potential φ from which **E** is obtained such that $\mathbf{E} = -\nabla\varphi$. The current density can be computed from the electric field by applying Ohm's law $\mathbf{J} = \sigma\mathbf{E}$. We assume the fluid domain was non-conductive and therefore, we disregard electro-kinetic effects within the fluid domain, and as such, Joule heating was only considered in the fiber skeleton. The unsteady temperature distribution was modeled using the unsteady energy equation:

$$\rho_s C_{ps} \frac{\partial T}{\partial t} = \nabla \cdot (k_s(T)\nabla T) + Q_h. \tag{8}$$

where ρ_s is the solid density, C_{ps} is the specific heat capacity, T is the temperature field, and k_s is the thermal conductivity. The above is non-linear, capturing the strong dependence of the thermal conductivity of the graphite fibers on temperature. The specific heat capacity and density were also modeled as a function of temperature. The source term Q_h represents the contribution of the Joule or ohmic heating to the unsteady temperature field. It is coupled directly to the energy equation after solving Equation 7 and is given by:

$$Q_h = \sigma(T)|\mathbf{E}|^2. \tag{9}$$

Q_h primarily drives the heating process and is strongly influenced by the direction of current and the material's microstructure. The boundary conditions used to solve Equation (8) are selected based on the operating conditions of a porous carbon paper heating element embedded within a quartz tube reactor such as in [9] and represented in Figure 3a. We limit the scope to characteristics within the RVE scale, and as such, the boundary conditions are as follows:

$$\begin{aligned} \varphi|_{y=0} = \varphi_0, \quad \varphi|_{y=L} = 0, &\qquad \text{on } \Gamma_{vD} \\ \nabla\varphi \cdot \mathbf{n} = 0, &\qquad \text{on } \Gamma_{vN} \end{aligned} \tag{10}$$

where **n** is the unit normal vector. An externally applied electrostatic potential value of φ_o was prescribed on the Dirichlet boundary Γ_{vD} normal to the *y* plane and a ground condition was applied on the opposite end. φ_o denotes the applied voltage pulse that drives the Joule heating with values ranging between 5.5 – 7.2 V applied, similar to voltage-to-distance ratios of 27.5 – 35 V/cm used in [9]. An insulation condition $\nabla\varphi \cdot \mathbf{n} = 0$ was applied on the boundary Γ_{vN} (i.e., other faces). For the temperature equation (Equation 8), the boundary conditions include:

$$\begin{aligned} -(k_s\nabla T) \cdot \mathbf{n} = q, &\qquad \text{on } \Gamma_{TN} \\ (k_s\nabla T) \cdot \mathbf{n} = 0, &\qquad \text{on } \Gamma_{TA} \end{aligned} \tag{11}$$

where Γ_{TN} and Γ_{TA} correspond to the surfaces associated with the prescribed heat flux and adiabatic conditions respectively. q represents the heat loss due to radiation q_r and convection q_c set along fiber surfaces. The total heat loss is represented as $q = q_c + q_r$. The convection losses are calculated from:

$$q_c = -h(T - T_{inf}), \tag{12}$$

And radiative heat losses from

$$q_r = -\varepsilon\sigma(T^4 - T_{inf}^4). \tag{13}$$

where h is the convection coefficient, T_{inf} is the ambient temperature (600 K in this case), σ is the Stefan-Boltzmann's constant, and ε is the emissivity.

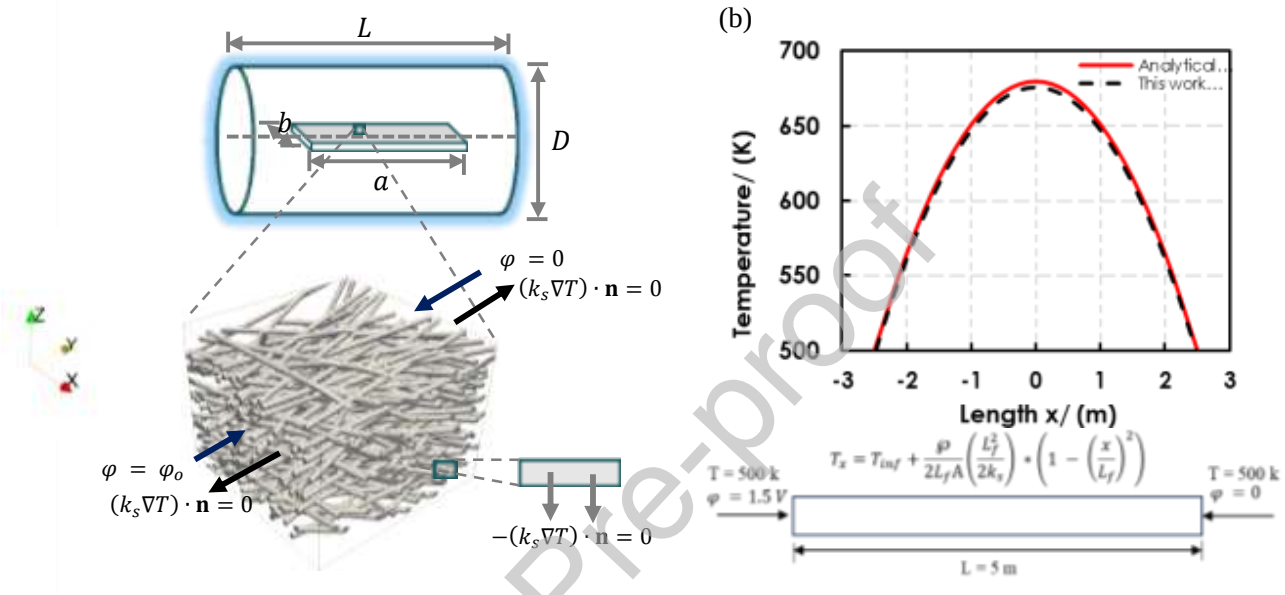

Figure 3: (a) Boundary conditions used for the electro-thermal analysis. Non-woven graphite fibrous reactor is assumed to be located within a vacuum tube and is heated via Joule heating. A representative volume element (RVE) from the sample was used for the modeling. (b) 1D verification of the model for a JH case without heat loss. Solid fiber with a square cross-section, A was heated by introducing $\wp = IV_x$ (current (I) times voltage (V_x)) across the fiber. The temperature distribution is displayed in the top figure.

We carried out one dimensional (1D) verification of the model before applying it for the simulations in this work (see Figure 3b). Moreover, the heating process from initial state to peak temperature is heavily dependent on convective and radiative heat losses. Radiation would be the predominant heat loss mechanism after about 1200 K based on preliminary energy conservation analysis. Below this temperature, convective heat losses would be prevalent. The convection coefficient was estimated for laminar gas flow past a cylindrical surface. The radiation model in this paper simulates the heat flux emitted without accounting for irradiation. This helps to simplify the model and reduces the computational effort. For cases of high temperatures, such as during quenching, the heat flux emitted, transmitted, and reflected by the surfaces would be incorporated in the embedded boundary system for studying dehydrogenation (future work). Using the embedded boundary method, the flux/Neumann condition can be discretized using the central difference scheme:

$$\frac{-q}{k_s} = \left(\frac{\partial T}{\partial n}\right) = \frac{T_I - T_{GL}}{\psi(\mathbf{x})} \tag{14}$$

where T_I is the temperature in the solid and T_{GL} is the temperature in the ghost layer. Moreover, to ensure that the interface, $\psi(\mathbf{x}) = 0$ is well captured and subsequently the heat loss computations with the EBM, an adequate grid resolution is required to resolve the fibers. Approximately 6 ± 2 grid points per fiber in all spatial direction were applied based on mesh analysis.

2.2.2 Solution and Analysis Approach

Equations (7) – (13) represent the complete unsteady Joule heating equation for the coupled problem. The partial differential equations were discretized on a second-order finite difference mesh. The solution scheme for the problem is illustrated in Figure 4. The problem is solved from initial time t_0 to $t_{cycle,n}$ where t_0 is the initial time and $t_{cycle,n}$ is total time for the PHQ including pulse and quenching steps for n cycles as seen in Figures 4b and 4c. The thermal and electrical domains were first initialized: 600 K in the thermal domain and 0 V in the electrical domain. The steady-state solution of the electric potential from Equation (7) is then obtained and used to solve for the current density, **J** and Joule heating volumetric term, Q_h by computing the gradient of electrostatic potential field. Q_h is coupled to the temperature equation as a source term for solving for the temperature fields.

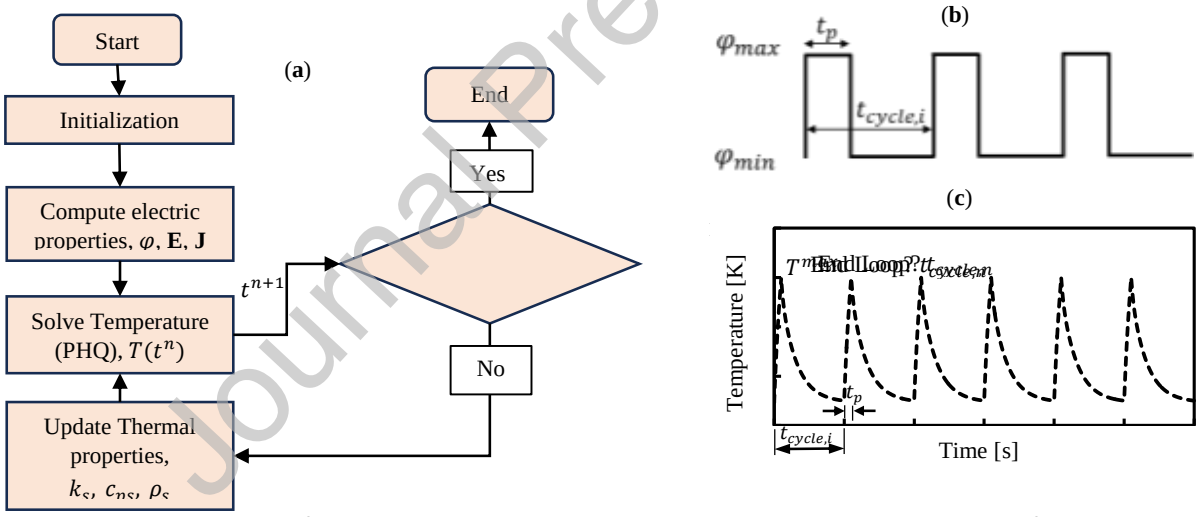

Figure 4: (a) Flow chart for solving the coupled Joule heating equations, (b) An example of a typical pulsed heating and quenching (PHQ) program where $\varphi_{min} = 0$ is applied under initial conditions and $\varphi_{max} = 7.2$ for t_p seconds from initial time to create the temperature response (c) before being switched "off" after t_p seconds.

The time-dependent temperature equation uses the same solution of Joule heating volumetric term Q_h as a source term at each time step to update the temperature which is then used to update temperature-dependent properties (k_s, c_{ps}, ρ_s) after each timestep. This happens until t_p is reached. Although, this workflow can be applied for a complete PHQ system by turning "off" the heat source after t_p is reached for one cycle, we only show the results for the pulse phase of a single cycle in this work. Moreover, heat

loss due to convection and radiation was computed using the embedded boundary method for capturing interfacial boundary condition on the structured mesh. The computational model was implemented within in-house code Quilt [23] developed at the Oak Ridge National Laboratory. We leveraged high-performance computing (HPC) for solving the equations due to the large number of grid points. 100 nodes were used on the Oak Ridge Leadership Computing Facility (OLCF) Summit computer to model the Joule heating problem. Our initial implementation of the model only used Summit's CPUs, while GPUs will be applied in future works. OpenMP thread parallelism was used with each thread bound to one processor. 40 processes per node were used through the computational domains and a topology of 20×20×10 of the cartesian communicator.

2.2.3 Simulation Parameters and Material Properties

The thermal and electrical domain properties used in this study are presented in Table 1. The thermal conductivity of graphite, with strong dependence on temperature, and specific heat capacity were modeled as functions of temperature. The correlations were based on data from existing literature on the material as shown in the table. The ambient temperature within the vacuum chamber was 600 K. Voltage pulses ranging from 5.5 V to 7.2 V were used to solve for the potential field. The transient problem was solved for one pulse with t_p = 20 ms without quenching. Due to the peak temperature range which we predicted a priori in this work, we did not account for fiber deformation or damage within the level set model due to graphite high sublimation temperatures (greater than 3600 K [25]) and low coefficient of thermal expansion ($1.0 \times 10^{-6}\ K^{-1}$).

Table 1: Material properties and simulation parameters.

Parameter	Value	Unit	Reference
ρ_0	1.4×10^{-5} (G4) – 3.5×10^{-5} (G1-G4)	[Ω.m]	[26]
h	100	[W/m^2 K]	-
ε	0.95	-	[9]
T_{inf}	600	[K]	-
φ_o	5.5 (G4) – 7.2 (G1-G4)	[V]	-
t_p	20	[ms]	-
ρ_s	$-3.5 \times 10^{-5}(T - 273.0) + 1.8916$	[g/cm^3]	[27]
k_s	$\begin{matrix} 2\times10^{-15}T^5 - 2\times10^{-11}T^4 + 6\times10^{-8}T^3 \\ -4\times10^{-5}T^2 - 0.0891T + 163.28 \\ 44.0 \end{matrix}\Bigg\}\begin{matrix} T \le 2373\ K \\ T > 2373\ K \end{matrix}$	[W/m.K]	-
c_{ps}	$(0.444 + 0.308\times10^{-4}T - 0.61\times10^{5}T^{-2} + 0.108\times10^{8}T^{-3} + 1.8916) * 4184$	[J/Kg.K]	[28]

2.3 Computational Domain

Fibrous packings akin to carbon felt – a non-woven carbon fiber network devoid of binder or resin were used for simulating Joule heating at the pore scale. They were computationally generated to capture the

statistical features of carbon felt thereby enabling a realistic representation of the domain using a few adjustable parameters. The digitally reconstructed fibrous skeleton was defined by the fiber diameter, porosity, and its orientation. The domain used for this study was obtained using stochastic model by Schladitz et al. [29]. It involves the use of a stationary Poisson line process with a one-parametric directional distribution used to determine the fiber directions while assuming fibers are isotropic in the in-plane (*x-y*) direction. The directional distribution can be expressed in the form of probability density in polar coordinates based on experimental characterization of carbon paper (Equation 15):

$$p_z(\theta) = \frac{1}{2}\frac{\beta \sin\theta}{(1 + (\beta^2 - 1)\cos^2\theta)^{3/2}}, \tag{15}$$

$$p_{xy}(\vartheta) = 1/2\pi\,. \tag{16}$$

where $p_z(\theta)$ and $p_{xy}(\vartheta)$ are the probability density functions of the polar angle – the inclination to the z-axis or through-plane(θ), and azimuthal angle – the angle in the *x-y* plane (ϑ) or in-plane respectively. The probability densities $p_z(\theta)$ and $p_{xy}(\vartheta)$ are independent and can be described by a combined probability $p(\theta,\vartheta) = p_z(\theta)p_{xy}(\vartheta)$ which results in the expression by Schladitz et al. [29]. The polar angle is valid in the range of [0, π) while the azimuthal angle ranges between [0, 2π). β regulates the anisotropy of the fiber packing by adjusting the variance of the polar angle. When $\beta = 1$, the fibers are isotropic. $\beta > 1$ results in the packing assuming an anisotropic microstructure with fibers becoming parallel to the *x-y* plane at high values of β. Moreover, the fibers were created by first obtaining a cumulative distribution function of PDFs p_z and p_{xy} from which inverse functions were derived. The inverse functions $p_z^{-1}(\zeta_\theta)$ and $p_{xy}^{-1}(\zeta_\vartheta)$ then take in randomly generated distributions of auxiliary variables ζ_θ and ζ_ϑ which are defined such that $\zeta \in [0,1)$ from which the θ and ϑ spaces are created. These values together with randomly generated position vectors are then used to characterize each fiber segment parallel to the principal axis as illustrated by Yiotis et al. [30]. In this work, the fibers were generated with ζ_θ within the range of 0 – 0.5 and ζ_ϑ from 0 – 0.32. The fibers were restricted to straight overlapping fibers with circular cross-sections and constant radius. Furthermore, to study the effect of the microstructure on the peak temperature during pulsed heating (PH), we varied the porosity, β, and fiber diameter of the porous media. This required the generation of four computational domain geometries – one base geometry with features similar to carbon paper/felt, and the other three varying either in porosity, fiber diameter or β. Details of the geometry properties are described in Table 2.

Table 2: Microstructural properties of domains for FJH simulations. Three main properties were varied – porosity ε, anisotropic factor β and fiber diameter, d and analyzed with the base case geometry G1.

	Porosity, ϕ (%)	Beta, β	Fiber diameter, d (μm)	Thickness (mm)	Number of Fibers	Avg. Fiber Length, l (mm)
Geometry 1 (G1)	80	5.0	10	1.0	5093	1.92

Geometry 2 (G2)	90	5.0	10	1.0	2547	1.90
Geometry 3 (G3)	80	1.0	10	1.0	5093	1.68
Geometry 4 (G4)	80	5.0	20	1.0	1273	1.902

The listed geometries can be visualized in Figure 5. The configurations of the fiber skeletons with an RVE of size 2.0×2.0×1.0 mm^3. The geometries were created stochastically using a *python* script on a local computer with a target porosity during generation to ensure that the properties of interest were obtained. For example, box G1 in Figure 5a, with a porosity of 80% required 5093 straight fibers with diameter 10 μm to fill up the void space. The porosity was later verified by integrating the fiber volume using the level set function. The final porosity varied slightly by 1.2% to 3.7% due to the interconnectivity of the fibers.

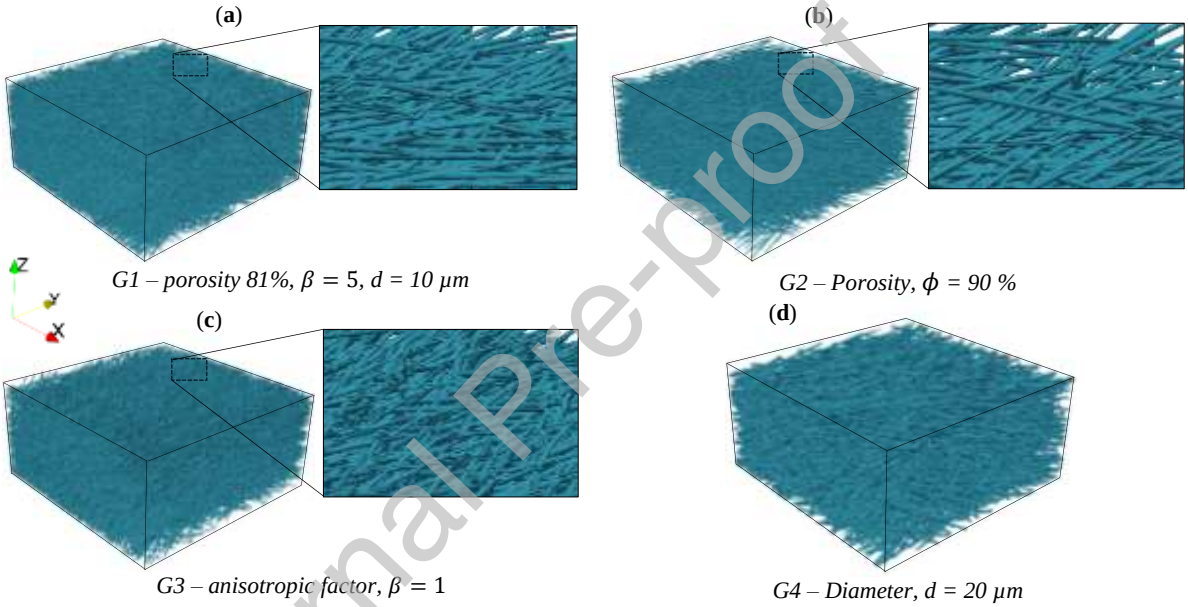

Figure 5: The stochastically reconstructed fiber packings/skeletons with a volume of 2.0×2.0×1.0 mm^3 used in this work. The domains are composed of straight fiber cylindrical networks with constant radius. (a) Base case – domain G1, (b) domain – G2 with higher porosity (lower packing density), (c) anisotropic domain, G3, (d) domain – G4 with diameter twice the base case.

Other geometries included one variation of this base geometry. G2 for instance had a variation in its porosity (ϕ = 90%), G3 varied in fiber orientation, ($\beta = 1$), while G4 had a fiber diameter variation (d = 20 μm). For carbon paper, $\beta = 5$ provides the closest match for the average probability density function (PDF) data experimentally [30] and was hence, used to represent the G1, G2, and G4 domains. The domain G3 in this paper was labeled anisotropic, although is defined as isotropic with respect to the *x-y* plane according to Equation 15. This is due to the presence of two fibers orientations – one parallel to the *x-y* plane and the other category includes fibers aligning to the *z* plane. Consequently, it had the smallest average fiber length as a large proportion of its fibers aligned in the thickness direction. Moreover, from Table 1, the domains with the most fibers were G1 and G3, while G4 had the lowest count of fibers due to

its larger fiber diameter while maintaining a porosity of 80%. The RVEs were discretized with a grid resolution of 2.78 μm in *x, y,* and *z* directions enabling the capturing of interfacial conditions of each fiber more accurately. This resulted in a total of 187 million grid points for each domain.

2.3.1 Fiber Analysis

To examine the effect of FJH on the microstructural properties, the local porosities were computed along the in-plane directions of the fibers. The results display a similar trend for all the geometries with the local porosity at the center of each geometry being identical to the bulk porosity for both *x* and *y* directions (Figure 6a and 6b respectively). The local values along both directions increased slightly at the edges due to the clustering of the fibers at the center during the fiber skeleton stochastic reconstruction process, thus increasing the fiber density. The converse was true for the local porosity at the boundaries being more sparsely distributed fiber due to fibers originating from different planes. The porosities at the boundaries for G2 had a porosity of 93.5% and 93.1% at the origin in the *x* and *y* directions respectively, indicating the fibers were distributed uniformly along both boundaries. This observation varied slightly at the opposite boundary with local porosities of 96% and 92% in the *x* and *y* directions respectively. As the number of fibers originating from, or terminating in the same plane direction increases, these boundary effects would reduce and vice-versa. Information on fiber orientation for the geometries was also obtained. Figure 7 illustrates the probability densities of the fiber orientation from the stochastically generated fibers. The plots in the first column, from top to bottom, are the probability density functions (PDFs) of all fibers in G1-G4 oriented in the *x* direction respectively while the plots in the second column are for PDFs of the fibers oriented in the *y* directions for G1-G4 accordingly, and the third column is for fibers oriented with respect to the z-axis for domains G1-G4. Higher values of the fiber orientation unit vector in the PDFs imply fiber connectivity, with a value of 1 denoting fibers that are fully connected and aligned orthogonal to the plane, while 0 describes fibers that are tangential and thus not connected. All the domains for nx/L_f and ny/L_f displayed uniform distributions up to 0.8 in line with Equation 16. Beyond 0.8, the probability density increased significantly based on additional criteria for fiber connectivity that were imposed on the model. For domains G1, G2, and G4, the large probability density of nz/L_f at 0 indicates that a large number of the fibers were tangential to the azimuthal plane as expected because they are isotropic. Domain 3 on the other hand had fibers generated for every nz/L_f configuration. The histogram has a mode of 0.0 demonstrating that a lot of the fibers are oriented parallel to the *x-y* plane while the rest align with the *z* plane making the packing anisotropic. Such information would be useful in understanding the effect of fiber connectivity on the current density and peak temperatures.

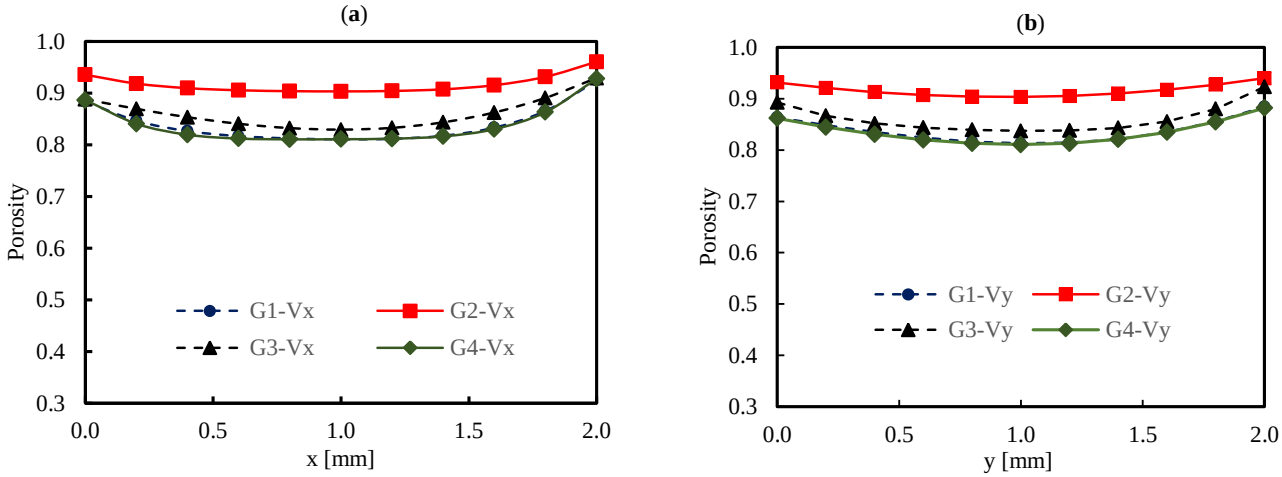

Figure 6: Distributions of the local porosities across the in-plane directions. (a) Local porosity in the x-axis direction, (b) local porosity in the y-direction.

3.0 Results and Discussion

3.1 Joule Heating in Pore-resolved Porous Media

3.1.1 Electrostatic Model Results

The results from the simulation of the electric field through the porous media were analyzed for all four representative geometries and described in Figure 8.

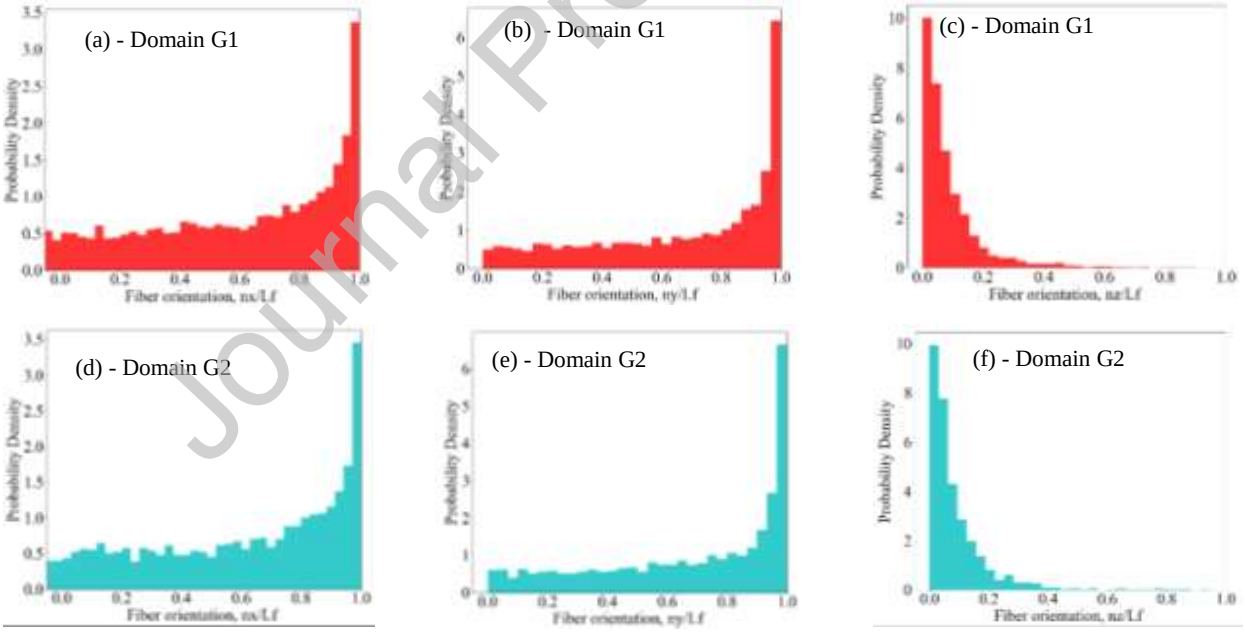

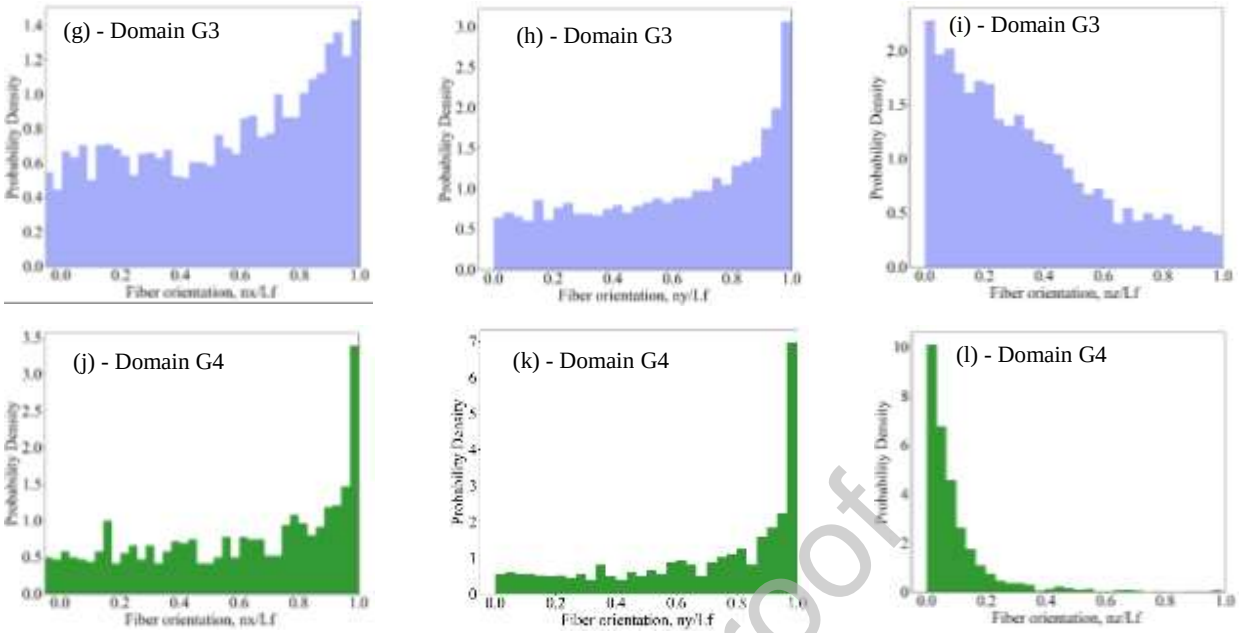

Figure 7: Probability density functions of the fiber orientation for all four geometries with respect to the x plane in the first column, while the middle column indicates the orientations with respect to the y plane accordingly, and the last column is for fibers with respect to the z plane.

Figures 8a-8d illustrate the electrostatic potential field results, as well as their corresponding current density plots (in Figures 8e-8h) for all geometries from G1 (left) up to G4 (on the right). The potential decreases linearly along the direction of applied voltage from left $\varphi|_{y=0}$ to right $\varphi|_{y=L}$ given that the electric conductivity is homogeneous throughout the domain, with the slope determined by the prescribed boundary conditions. Moreover, the plot of the current density **J** magnitude in Figures 8e-8h display non-uniformities due to the variation in structural features such as the fiber connectivity, anisotropy and direction of applied voltage (current flow). Fibers oriented along the *y* plane had **J** magnitude values greater than 30 A/mm^2 whereas fibers oriented in the lateral direction (connected across the *x* plane) had values less than 10 A/mm^2. This result was further examined using histograms normalized by probability densities in Figure 9.

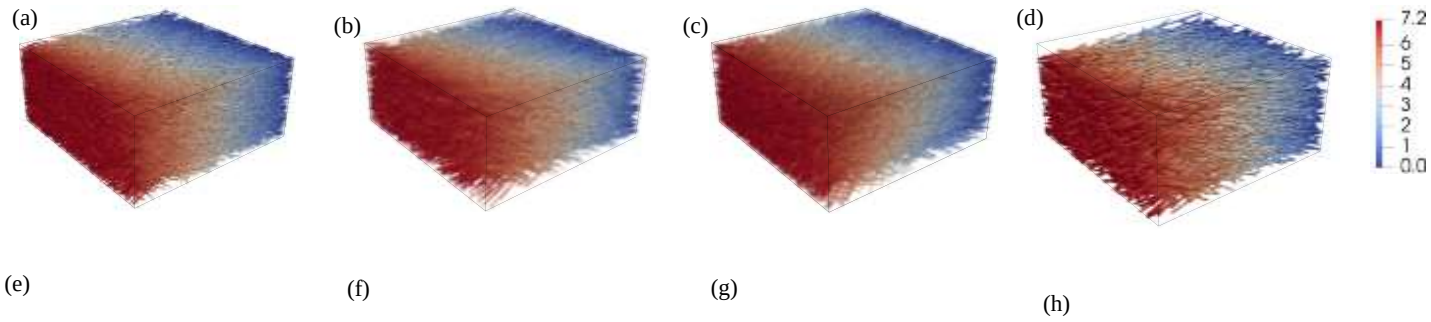

(e) (f) (g) (h)

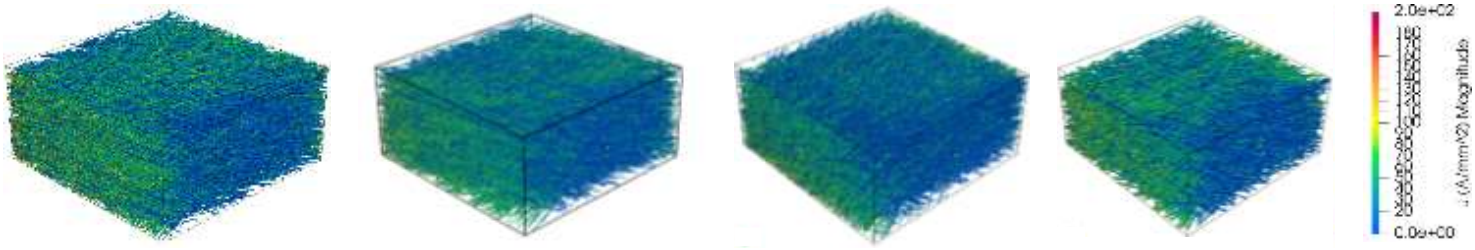

Figure 8: (a) Electric Potential distribution for domain G1, (b) domain G2, (c) domain G3, and (d) domain G4, and their respective current density 3D plots in (e) – (h). The current density within the fibers will induce Joule heating.

The plots in Figures 9a-9d show a log-normal distribution with a mode of 1.0 for all the geometries indicating that probability densities of **J** within fibers normal to the *y* plane were the largest. This information provides a close correlation with the fiber connectivity in Figures 7b, 7e, 7h and 7k which gives insights into fiber connectivity probability densities in the azimuthal direction. Furthermore, G3 in Figure 9c had the lowest probability density at the mode (~ 4) whereas other domains had values of 7 or greater. This is attributed to anisotropy within the domain, implying that the distribution of the fibers oriented in the thickness direction provided increased electrical resistance and thus less current flowing the domain. Moreover, we also observed some negative values of $\hat{\mathrm{J}}_{\mathrm{y}}$ in Figure 9. This is due to the "back-flow" of current in fibers intersecting or touching in the opposite direction of current flow. This effect, however, only occurred in a small fraction of the fibers and hence, did not impact the average temperature significantly. The volumetric heat source normalized by the square of the electrostatic potential gradient – $\dot{Q}_y$ was also quantified and illustrated in Figure 10a to further elucidate the effect of the microstructure on electro-thermal quantities. $\dot{Q}_y$ is defined as:

$$\dot{Q}_y = \sum_{k}^{nz} \sum_{i}^{nx} Q_{h,ik} \left(\frac{L_y}{\varphi_0}\right)^2, \tag{17}$$

where nx and nz are the number of grid points in the *x* and *y* axes respectively, and L_y is the length in the *y*-direction. A second measure $\dot{Q}_{yo}$ is defined as:

$$\dot{Q}_{yo} = \sum_{k}^{nz} \sum_{i}^{nx} Q_{h,ik} \frac{1}{\psi_{ik}} \left(\frac{L_y^2}{\sigma \varphi_0^2}\right). \qquad \psi > 0 \tag{18}$$

where $\dot{Q}_{yo}$ (see Figure 10b) shows the distribution of the normalized Joule heating source term across the geometries. ψ_{ik} is the sum of the distance function values on the fiber at a given plane. $\dot{Q}_{yo}$ provides a weighted representation of $\dot{Q}_y$ that puts an emphasis on the effect of the level set function on the heat source term. This effect is highlighted in Figure 10 where G2 provides an underestimation of Q_h in Figure 10a compared to 10b. $\dot{Q}_y$ is however would be useful in providing information on the overall heat

generation in the entire system if both regions were conductive which is not the case here. The effect of porosity can be seen in Figure 10b which reveals a drop in $\dot{Q}_{yo}$ due to the presence of more void spaces within the domain limiting conductive pathways for current flow. The profiles of G1 and G4 are similar when y/L > 0.35 despite differences in fiber diameter. $\dot{Q}_{yo}$ was also highest toward the left of the domain where electrostatic potential was applied and dissipates across the media but increases slightly at the y/L. The drop in $\dot{Q}_{yo}$ can be explained by the reduction in local porosity at the middle of the domains due to the convergence of fibers originating from other planes as explained in section 2.3.1. Although, the local porosity increases at the center, electric current dissipates into other fibers in the lateral and *z*-direction leading to a lower $\dot{Q}_{yo}$ This effect, however, reduces at the opposite boundary as the local porosity increases and we see a slight increase in $\dot{Q}_{y}$. Moreover, it is worth noting that the simulation convergence times for solving the electrostatic field Equation (7) was affected by the nature of the geometry. The computation for G1 converged after 1,212,800 iterations, G2 after 1,291,200 iterations, G3 after 1,348,800 iterations and G4 after 1,405,000 iterations.

3.1.2 Temperature Results

During simulation, the electric current flow within the carbon felt conductor was kept "on" for the entire duration of the pulsed heating which ran from initial time $t = t_0 = 0$ to $t = t_p$ ms implying that Q_h from the steady state Equation (7) was coupled at every timestep to the energy equation. The temperature transients across selected grid points during the Joule heating are shown in Figure 11. The points were selected from the top surface of the geometry (z = L_z), or close to it, at five different sections located at pre-determined distances – in this case, one-fifth of the length of each domain away from the edge of interest (P1, P2, P3, P4) and at the center of the domain (P5) and the temperatures were recorded during the simulation. Figures 11a-11d, illustrate transient temperature profiles that increased uniformly from t_0 to t_p. In all cases, the temperatures at the points closest to $\varphi|_{y=0}$ were the highest (i.e., P1 and P2) whereas temperatures at points located near boundary $\varphi|_{y=L}$ were the lowest. Temperatures at points P3 and P4 in all geometries at t_p were identical having a small temperature range except for G4 (Figure 11d) which had temperatures varying by almost 16%. The temperatures for domain G3 (Figure 11c) were the most heterogenous with local temperatures at P1-P3 being more spread out than for other domains, reflective of the diversity in its microstructure. Moreover, 3D plots of the temperature are also shown in Figure 12 at t_p. Joule heating in the fiber skeletons due electric field generation can be observed across the entire domain. The top row of the figure indicates a 3D view of the packing with the positive *z* direction facing upwards and second row is the bottom of the sample with the positive *z* direction facing

downwards. In all cases, the heating was non-uniform with the highest temperature regions (1800 K and above) located around the bottom left corner (0,0,0) of the domains.

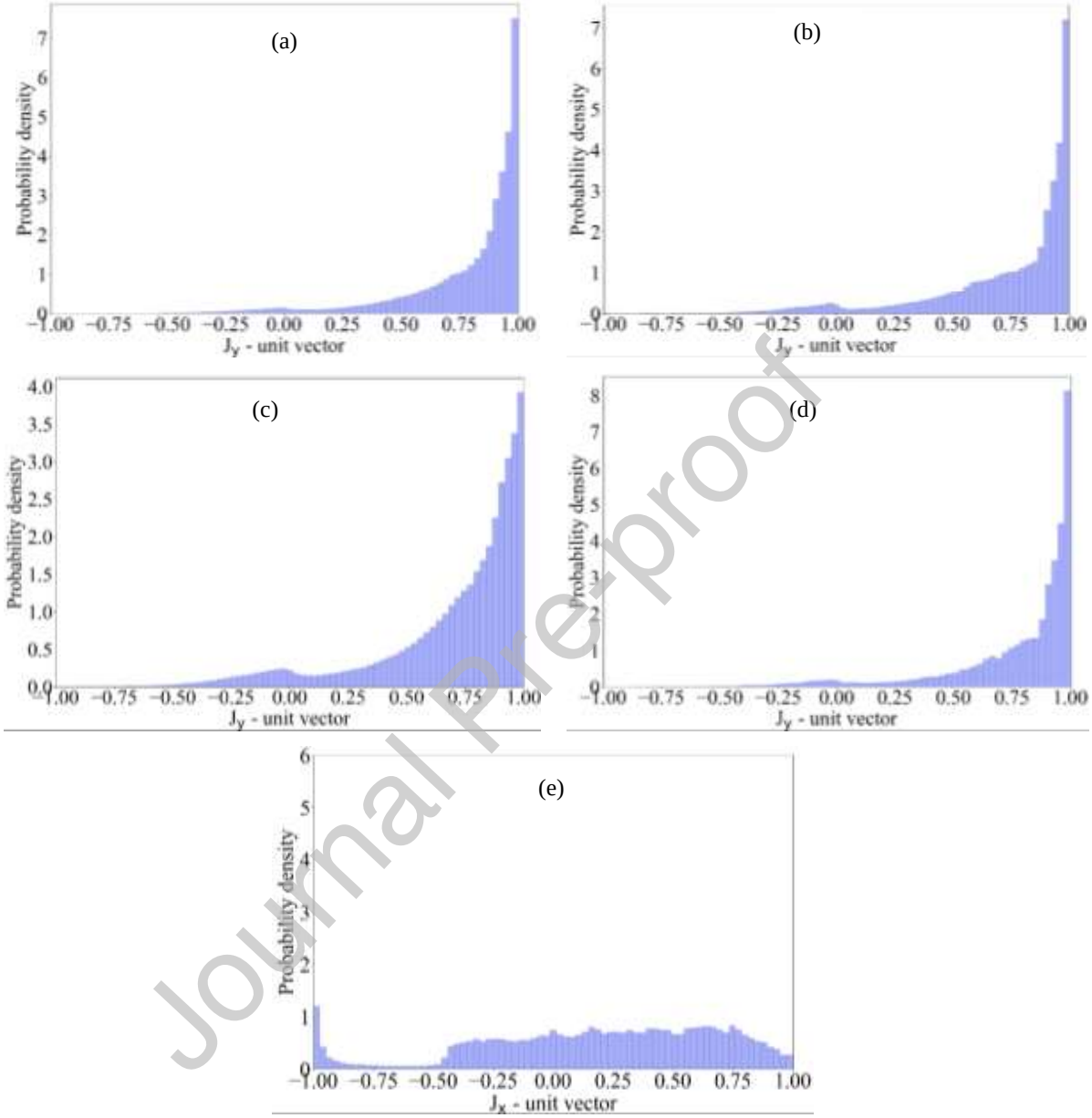

Figure 9: Normalized histograms of current density J for G1, G2, G3 and G4 in (a) – (d) respectively. The mode for (a)-(d) are 1.0 indicating the largest distribution of the current density within the connected fibers. (e) Normalized histogram for $\hat{J}_x$ for domain G4.

These high-temperature regions form possibly due to the large cluster of fibers around the origin during the stochastic fiber generation leading to a large concentration of electric charges in that section. Fibers branching out in the *x*-direction, however, experienced lower temperatures due to the lower probability

density of $\hat{J}_x$ implying that there is less electric current flow in that direction. This temperature non-uniformity is further compounded by anisotropy (see Figure 9d) – fibers oriented in the thickness direction do not contribute significantly to the flow of current in the axis where the voltage was prescribed. This resulted in the temperatures of fibers on $T|_x$ displaying low temperatures – less than 1200 K. Temperature results were also analyzed using normalized histograms (see Figure 13).

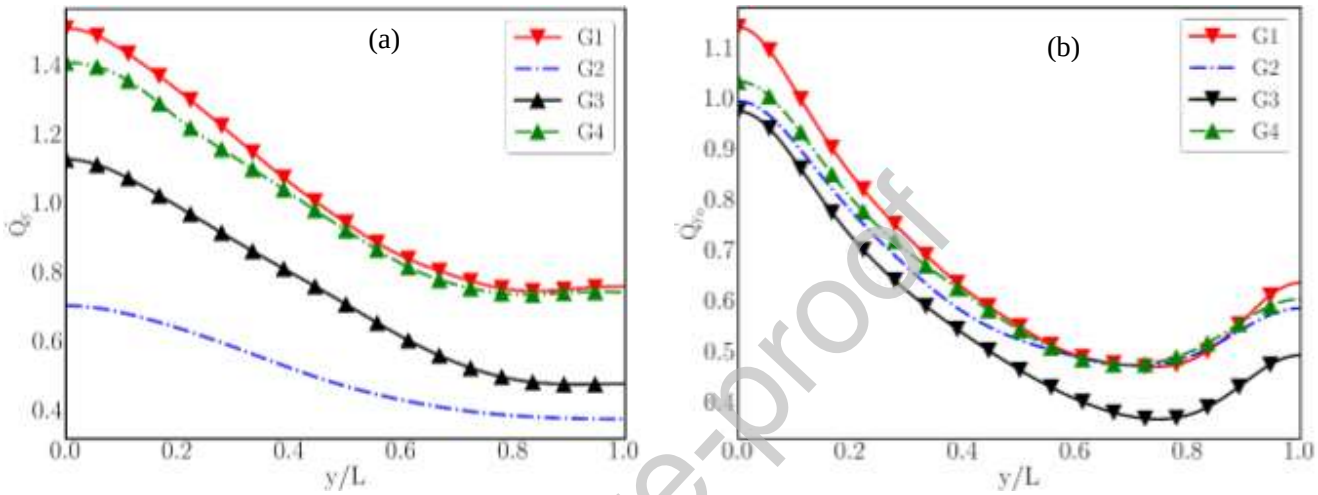

Figure 10: (a) A plot of normalized volumetric heat source term, $\dot{Q}_y$ plot along the y-direction averaged in the x-z plane.(b) Weighted heat source representation with level set distance function.

The largest mean/average temperature for domain G4 was 1700.9 K. This represented an increase in the mean temperature by 3.9% with respect to the base geometry G1. The lowest mean temperature was 1437.7 K for domain G3 denoting a reduction in mean temperature by 12.1%. Domain G4 also had the largest standard deviation (230.14 K) and peak temperature of 2525 K indicative of large temperature gradients within the fiber skeleton. The increase in peak and average temperatures in G4 was attributed to the increase in conductance as a result of its larger cross-sectional area which improved current flow allowing for the temperatures to be increased. Domain G2 on the other hand had the smallest deviation (181.2 K). It had a 4.7% reduction in average temperature due to its high porosity. The summary of the statistical results for the fiber parameters, current density and temperatures are described in Table 3. The average temperatures across the length of the domains in the *y*-direction are also shown in Figure 14. In all cases, the temperature remained uniform at the beginning of the Joule heating process (at t_0) but increased rapidly after just 5 ms due to the Joule heat generation and increases monotonically up to t_p for all geometries. The temperature is highest toward the left of the domain based on distribution of the volumetric heat source in Figure 10. Experimental validation was also carried out our model. We compared peak temperatures from Dong et al. [9] with our model under similar conditions using a box

plot. The peak temperatures for an average of voltage-to-distance ratios of 30 V/cm (at the left) and 35 V/cm (at the right) in Figure 15. The peak temperatures were similar in both cases. More accurate matches were not attained due to experimental uncertainties from occurrences such as clipping on the edge on carbon felt/paper and temperature measurements.

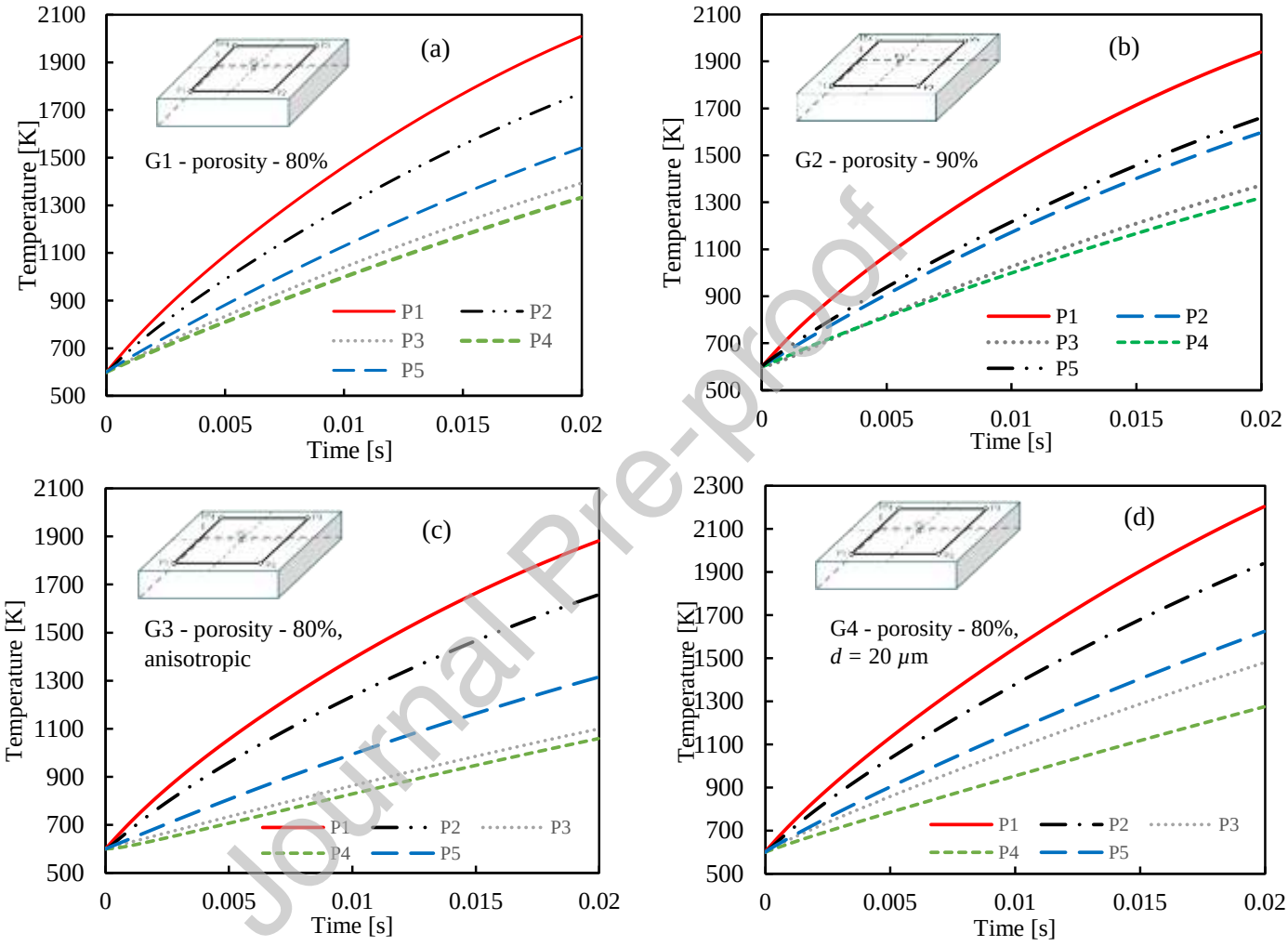

Figure 11: Temperature profiles for the heating phase of one PHQ cycle. Temperatures for domain G1 (a), domain G2 (b), domain G3 (c) and domain G4 (d) were probed across 5 points on top of the porous media in the positive z-direction. Probe points P1-P4 were selected from a fifth of the distance from the nearest edge while P5 was selected from the center of each domain.

3.2 Parametric Study

Parametric studies were carried out to further examine the effect of fiber skeleton microstructure and electrical properties on peak temperatures. To accomplish this, a range of potentials and resistivities were applied within the coupled system. A voltage pulse of 5.5 V was applied to domain G4 with resistivities of 1.4×10^{-5} and 3.5×10^{-5} Ω.m for different t_p values. They were labeled domain G4b and G4c

respectively. Additionally, stochastically generated fiber skeleton labeled domain G1b was generated to investigate the effect of the fiber connectivity on peak temperature.

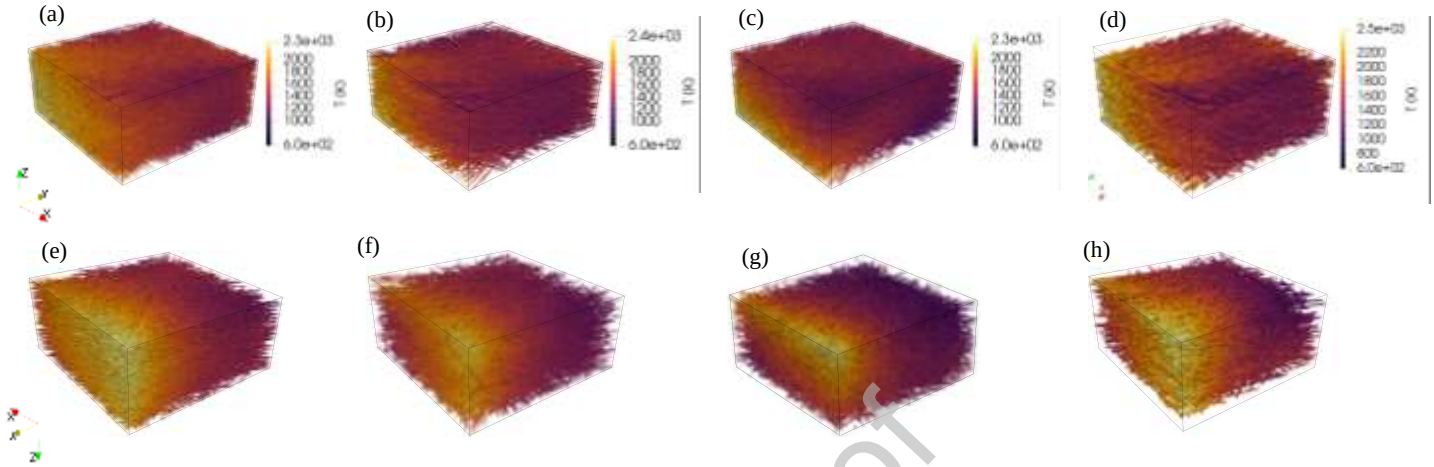

Figure 12: 3D plots of the temperatures at the end of pulsed heating, i.e., at t_p for G1 (a), G2 (b), G3 (c) and G4 (d). The top row represents the temperature plots in the upright position, i.e., the positive z-axis facing up while the bottom rows (e)-(h) are the G1-G4 domains respectively, flipped – negative z-axis on top.

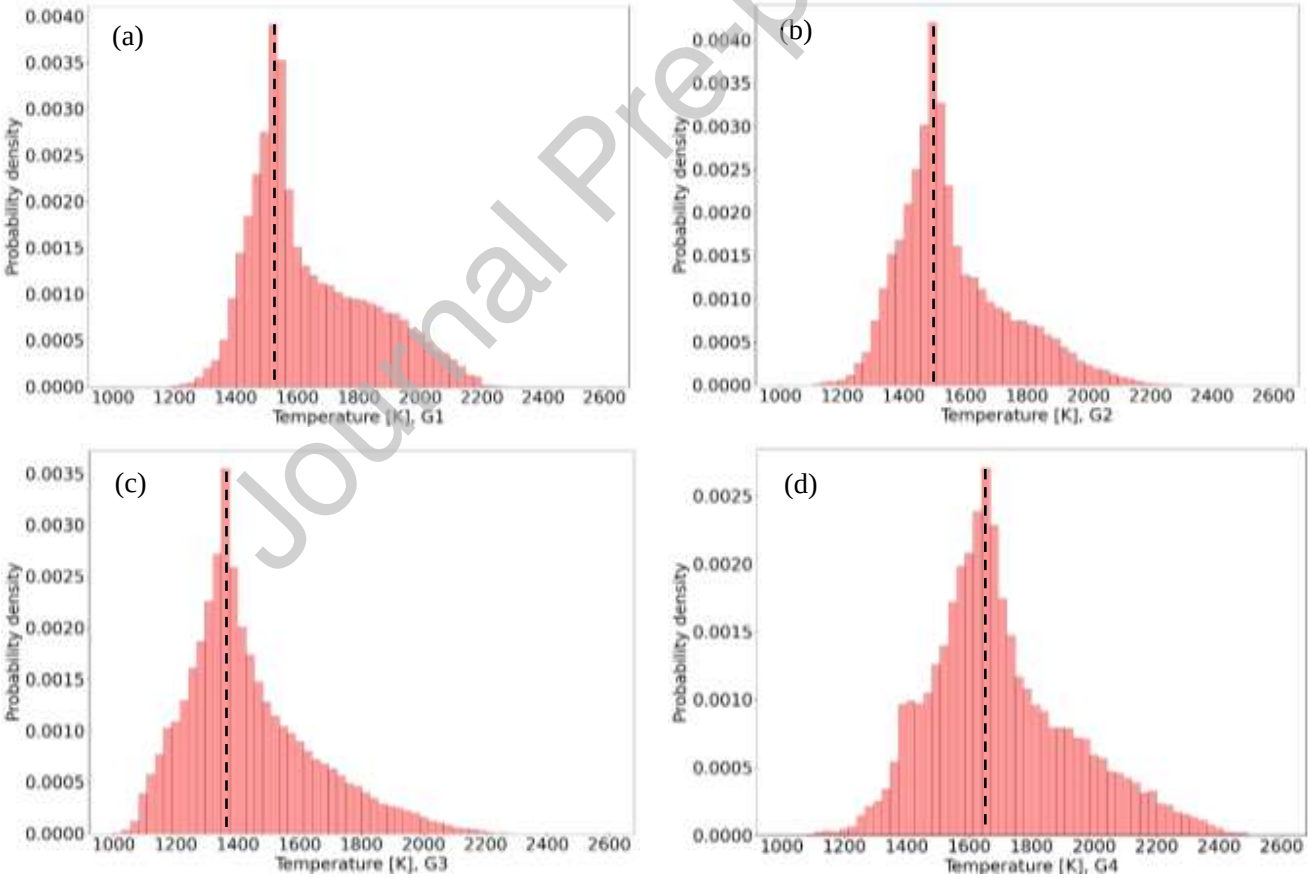

Figure 13: Histograms of temperature normalized by probability density for porous media G1 (a), G2 (b), G3 (c) and G4 (d) at t_p. The black dashed line represents the modes of the plots.

Table 3: Summary of PDFs for the FJH simulations – temperature, current density, and fiber orientation properties.

Geometry	Fiber Parameters (*y*-axis)		Current Density, J_y (A/mm^2)		Temperature (K)	
	Mean	Deviation	Mean	Deviation	Mean	Deviation
G1	0.66	0.27	62.7	39.4	1636.2	196.3
G2	0.66	0.27	58.6	40.6	1559.7	181.2
G3	0.61	0.28	49.9	39.4	1437.7	208.1
G4	0.67	0.28	62.1	40.2	1700.9	230.14

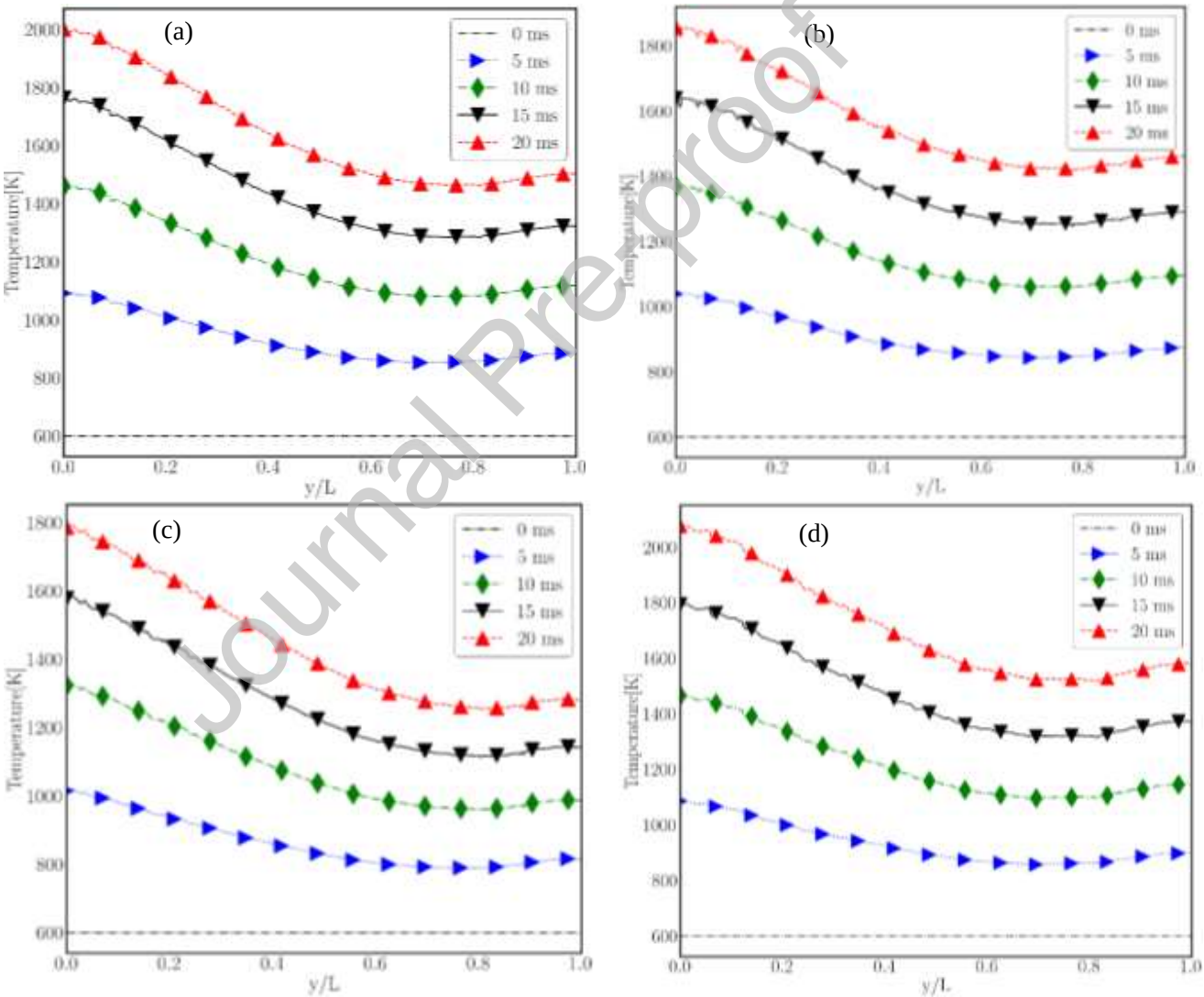

Figure 14: Average temperatures across the length of the domains in the y-direction for G1 (a), G2 (b), G3 (c) and G4 (d) at different times for an input voltage $\varphi|_{y=0}$ *of 7.2 V.*

This was achieved by reducing the range of auxiliary parameter ζ_ϑ for domain G1 from a maximum value of 0.32 to 0.25. This helped to generate fibers inclined at $\vartheta = 0$ to $\pi/2$. Details of the operating parameters are described in Table 4 along with the resulting peak temperatures. The result of the temperature distributions for cases G1b and G4b are shown in Figures 16a and 16b respectively while their corresponding probability density are illustrated in Figures 16c and 16d respectively.

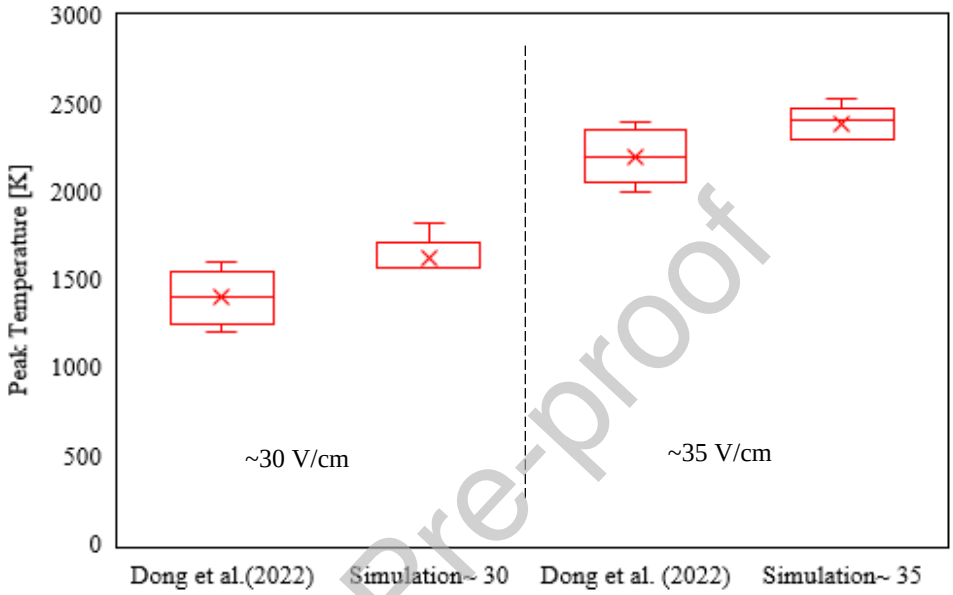

Figure 15: Box plot indicating experimental validation of the simulations. The first two plots (from the left) indicate peak temperatures from experiment and simulation (second figure) for an average voltage-to-distance (VDR) ratio of 30 V/cm while the two plots (on the right) are for VDR ~35 V/cm. The experimental values are temperatures resulting from voltages of 55-64 V applied for VDR ~30 V/cm and 67-72 V for VDR ~35 V/cm both at t_p=20 ms. The values for the simulation are the peak temperature ranges resulting from the different microstructures relating to each corresponding VDR.

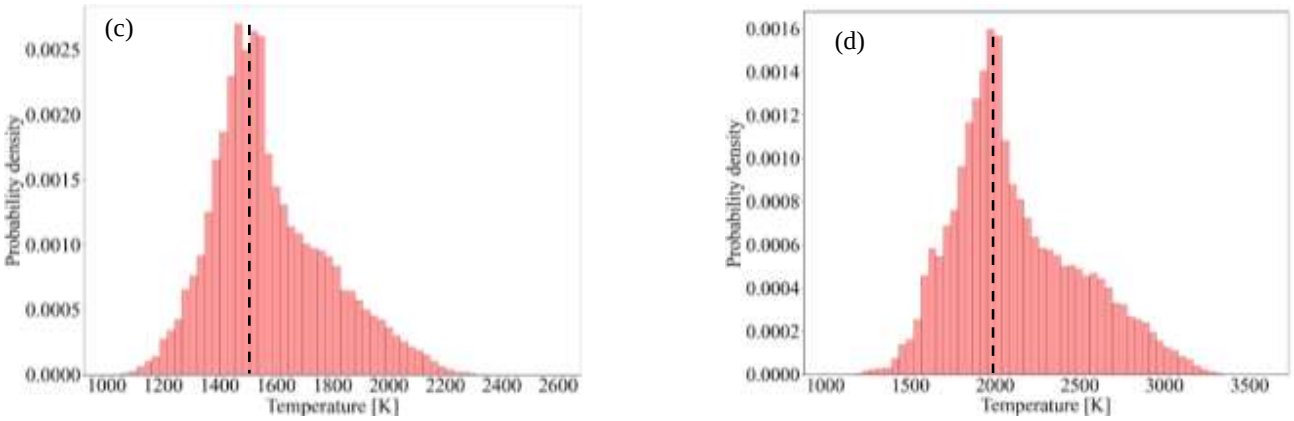

Figure 16: (a) and (c) Temperature and histogram of temperature normalized by the density of domain G1b respectively having a voltage pulse of 5.5 V with a mean of 1575.9 K, and deviation of 205.5 K. (b) and (d) Temperature and normalized histogram of temperature for domain 4b respectively having a voltage pulse of 5.5 V along and resistivity of 1.4×10^{-5} Ω.m with a mean of 2123.7 K and deviation of 376.4 K. Dashed line is the mode.

Table 4 also includes the results of the peak temperatures and compares their results with G1-G4. It can be seen that improving fiber connectivity, as with G1b, led to an increase in the peak temperature by 4.8%, albeit the average temperature was reduced by 3.7%. This indicates that fiber connectivity may increase the peak temperature but may not necessarily lead to an increase in average temperature. Moreover, domain G4b had the highest peak and average temperature (i.e., 3373 K and 2123.7 K respectively) due to a larger electrical conductivity. These peak temperatures are similar to the peak temperatures in experiment conducted by [9]. In the next section, peak temperature results from our pore scale model are compared with results from a ohmic heating approximation.

3.2.1 Peak Temperature Approximation

Theoretically, if we assume adiabatic conditions, constant current density, and no cooling or contact with a substrate, we can approximate the unsteady Joule heating equation after a single electric pulse with the following expression;

$$\frac{dT}{dt} \approx \frac{\Delta T}{\Delta t} = \frac{q_h}{\rho_s c_{ps}}. \tag{19}$$

where $q_h = \sigma\left(\varphi_0/L_y\right)^2$. In this case, the temperature distribution is dominated by Ohmic heating, and the temperature is the same across all fibers. This expression can give quick estimates of the peak temperature when designing experiments, however, it ignores microstructural information, heat loss, and the effect of diffusion and thus may lead to erroneous results depending on the model complexity. In this section, we compare the peak temperatures from our simulations with those from the approximation and we recommend scenarios where the approximation in Equation 19 could be applied to a porous material. With $\Delta t = t_p$, $c_{ps} = 2060$ J/kg.K, $\rho_s = 1890$ kg/m^3 and an initial temperature equal to 600 K, we computed the peak temperatures of each domain configuration in Table 4 and we compared the results

with the solutions from our transient model. The results indicated that peak temperature variations for the heat expression for domains G1, and G3 were the largest with a relative error of 8.9% and 9.1% respectively. However, as the connectivity of the fibers increased (i.e., domain G1b), the error reduced to 3.9%.

Table 4: Peak temperature results with effects of diffusion and heat sink from simulation compared with temperature approximation.

Geometry	Operating Parameters			Peak Temperature		
	Pulse width (ms)	Voltage (V)	Resistivity $\times 10^{-5}$ (Ω.m)	Theoretical Temperature (K)	Simulated Peak temperature (K)	Relative Error (%)
G1	20.0	7.2	3.5	2502.1	2298.2	8.87
G1b	~20.0	7.2	3.5	2502.1	2407.6	3.92
G2	20.0	7.2	3.5	2502.1	2416.8	3.53
G3	20.0	7.2	3.5	2502.1	2293.2	9.11
G4	20.0	7.2	3.5	2502.1	2525.7	-0.94
G4b	20.0	5.5	1.4	3374.8	3373.1	0.05
G4c	20.0	5.5	3.5	1709.9	1825.7	-6.34

This occurs due to improved flow of electric current through the packing, yielding higher temperatures within the domain. The simulated peak temperature of G4 at 2525.7 K however only had an error of -0.9%. When the voltage was reduced to 5.5 V with a resistivity of 1.4 $\times 10^{-5}$ Ω.m, the error was reduced to 0.05%. This indicates that the theoretical expression could provide better peak temperature estimates for domains containing thicker fibers. It should also be noted that the peak temperature for cases G4 and G4c exceeded the theoretical peak temperature. This suggests that when fiber diameter reaches a critical diameter $d^{\alpha}$the temperatures may exceed the theoretical value and the extent of the increase depends on the properties of the material.

4.0 Conclusions

We developed an electro-thermal model for carrying out Joule heating simulations in a graphite reactor at the pore scale. The model was discretized on a second-order finite difference mesh with the domains implicitly represented using a static level set framework. Convective and radiative losses were modeled using an embedded boundary technique for interpolating the temperature values at the interfacial boundaries. The pore scale modeling approach for such a system helped to provide valuable insights into how the heating of fibers at such a scale may be used to study complex physical and chemical phenomena. Particularly, we observed that heating due to Ohmic effects for the fiber-resolved graphite conductor will result in local temperature heterogeneity which is driven by non-uniformity of current density through the material. Moreover, the model was also used to investigate the effects of structural

features on Joule heating. We examined the effect of structural features such as porosity, fiber diameter, fiber orientation, anisotropy, and fiber connectivity on current density, average, and peak temperatures by reconstructing five fiber skeletons stochastically that mimic non-woven carbon paper. The simulations showed that the fiber microstructure played a crucial role in the temperature response. The conclusions were that:

1. Geometries with large fibers (~ 20 μm) had high average and peak temperatures with the mean temperature increasing by 3.9% while the peak temperature increased by 9.9 % in comparison to a base geometry with a 10 μm fiber diameter. Such fibers were able to conduct more electricity due to their larger cross-sectional areas, thus generating more heat.
2. Domains with fiber orientations that were anisotropic had the lowest mean and peak temperatures with a peak temperature of 2293 K and mean values of 1437.7K. They also had the largest standard deviation (230.14 K). The reduction in temperatures represented a 12.1% drop in average temperature and a drop in 5.1% for the peak temperatures.
3. An increase in porosity from 80% to 90%, however, led to an increase in the peak temperature by 5.1%. The mean temperature on the other hand reduced by 4.7%.
4. We also compared results with a simplified expression that only considers Ohmic effect on the transient heating with our simulation result.
    a. The approximate model over-predicted the temperatures for most of the cases because it did not incorporate the effects of diffusion, heat loss, and temperature-dependent properties.
    b. The model, however, produced small errors for fiber skeletons that were highly connected in the direction of current flow and for geometries with large fiber diameters.
    c. For fibers with fiber orientations that were anisotropic, the errors were as large as 9.1%. Predictions with the least errors were for packings with large fiber diameters due to high conductance. The errors, however, became negative as fiber diameter increased implying that the simulated value exceeded the theoretical value as the diameter approached a critical value.

Going forward, this electro-thermal framework will be expanded and applied for modeling catalysis of organic substances, particularly alkane dehydration. Computationally, the work would be expanded further to run on GPUs to reduce computational time.

5.0 Acknowledgements

This work was supported by the U.S. Department of Energy, Office of Science Energy Earthshot Initiative, as part of the NEETER EERC. This research used resources of the Oak Ridge Leadership Computing Facility, which is a DOE Office of Science User Facility supported under Contract DEAC05-00OR22725.

6.0 References

[1] L. Song, L. Yu, C. Brumme, R. Shaw, C. Zhang, and X. Xuan, "Joule heating effects on electrokinetic flows with conductivity gradients," *Electrophoresis*, vol. 42, no. 7–8, pp. 967–974, Apr. 2021, doi: 10.1002/ELPS.202000264.

[2] D. Zheng, Z. Qi, Z. Geng, W. Huang, G. Li, and F. Zhang, "Regulating the ion migration pathways to enhance Joule heating effect and dense nonaqueous phase liquid removal using pulsed direct current," *J Clean Prod*, vol. 508, p. 145586, May 2025, doi: 10.1016/J.JCLEPRO.2025.145586.

[3] M. K. D. Manshadi, A. Beskok, M. K. D. Manshadi, and A. Beskok, "Competing effects of buoyancy-driven and electrothermal flows for Joule heating-induced transport in microchannels," *Flow*, vol. 3, p. E23, Jul. 2023, doi: 10.1017/FLO.2023.19.

[4] J. Pan *et al.*, "Joule heating and electroosmotic flow in cellular micro/nano electroporation," *Lab Chip*, vol. 24, no. 4, pp. 819–831, Feb. 2024, doi: 10.1039/D3LC00568B.

[5] H. I. Mohammed, P. Talebizadehsardari, J. M. Mahdi, A. Arshad, A. Sciacovelli, and D. Giddings, "Improved melting of latent heat storage via porous medium and uniform Joule heat generation," *J Energy Storage*, vol. 31, p. 101747, Oct. 2020, doi: 10.1016/J.EST.2020.101747.

[6] L. Zheng, M. Ambrosetti, and E. Tronconi, "Joule-Heated Catalytic Reactors toward Decarbonization and Process Intensification: A Review," *ACS Engineering Au*, vol. 4, no. 1, pp. 4–21, Feb. 2024, doi: 10.1021/acsengineeringau.3c00045.

[7] S. G. Prolongo, R. Moriche, G. Del Rosario, A. Jiménez-Suárez, M. G. Prolongo, and A. Ureña, "Joule effect self-heating of epoxy composites reinforced with graphitic nanofillers," *Journal of Polymer Research*, vol. 23, no. 9, Sep. 2016, doi: 10.1007/s10965-016-1092-4.

[8] J. Yuan, Y. Zhang, F. Chen, and Z. Gu, "An overview of Joule heating in energy storage materials and applications," *J Mater Chem C Mater*, 2024, doi: 10.1039/d4tc01736f.

[9] Q. Dong *et al.*, "Programmable heating and quenching for efficient thermochemical synthesis," *Nature*, vol. 605, no. 7910, pp. 470–476, May 2022, doi: 10.1038/s41586-022-04568-6.

[10] L. Zhan, Z. Han, Q. Shao, M. L. Etheridge, T. Hays, and J. C. Bischof, "Rapid joule heating improves vitrification based cryopreservation," *Nat Commun*, vol. 13, no. 1, Dec. 2022, doi: 10.1038/s41467-022-33546-9.

[11] R. Guedert, D. L. L. S. Andrade, J. R. Silva, G. B. Pintarelli, and D. O. H. Suzuki, "Dynamic model of tissue electroporation on the basis of biological dispersion and Joule heating," *J Appl Phys*, vol. 135, no. 9, p. 95109, Mar. 2024, doi: 10.1063/5.0196390/19715358/095109_1_5.0196390.PDF.

[12] T. Kotnik, L. Rems, M. Tarek, and D. Miklavcic, "Membrane Electroporation and Electropermeabilization: Mechanisms and Models," *Annu Rev Biophys*, vol. 48, no. Volume 48, 2019, pp. 63–91, May 2019, doi: 10.1146/ANNUREV-BIOPHYS-052118-115451/CITE/REFWORKS.

[13] F. Guo, X. Nie, J. Sun, Y. Zhang, and J. Hong, "Simulation Study of the Influence of Joule Heating on Single-Cell Electroporation Under 10Hz IRE Pulses," *Proceedings - 2023 China Automation Congress, CAC 2023*, pp. 1091–1095, 2023, doi: 10.1109/CAC59555.2023.10450986.

[14] H. Fangohr, D. S. Chernyshenko, M. Franchin, T. Fischbacher, and G. Meier, "Joule heating in nanowires," *Phys Rev B Condens Matter Mater Phys*, vol. 84, no. 5, Aug. 2011, doi: 10.1103/PhysRevB.84.054437.

[15] C. M. Y. Claassen, M. W. Baltussen, E. A. J. F. Peters, and J. A. M. Kuipers, "An improved ghost cell Immersed Boundary Method for conjugate mass and heat transport in fluid-particle systems," *Chem Eng Sci*, vol. 291, p. 119936, Jun. 2024, doi: 10.1016/J.CES.2024.119936.

[16] A. A. Zaidi, "Heat transfer analysis in particle-laden flows using the immersed boundary method," *Particuology*, vol. 90, pp. 394–403, Jul. 2024, doi: 10.1016/J.PARTIC.2024.01.005.

[17] A. Singh and N. Kumar, "Coupled nodal integral-immersed boundary method (NI-IBM) for simulating convection-diffusion physics," *J Comput Phys*, vol. 519, p. 113394, Dec. 2024, doi: 10.1016/J.JCP.2024.113394.

[18] R. Mittal and R. Bhardwaj, "Immersed boundary methods for thermofluids problems," *Annual Review of Heat Transfer*, no. 24, 2021, Accessed: May 22, 2025. [Online]. Available: https://www.dl.begellhouse.com/references/5756967540dd1b03,3ae07302147f45b7,2e0aa8eb280d726b.html

[19] O. Desjardins, V. Moureau, and H. Pitsch, "An accurate conservative level set/ghost fluid method for simulating turbulent atomization," *J Comput Phys*, vol. 227, no. 18, pp. 8395–8416, Sep. 2008, doi: 10.1016/j.jcp.2008.05.027.

[20] S. Osher and J. A. Sethian, "Fronts Propagating with Curvature-Dependent Speed: Algorithms Based on Hamilton-Jacobi Formulations," *J Comput Phys*, vol. 79, pp. 12–49, 1988.

[21] C. S. Peskin, "The immersed boundary method," *Acta Numerica*, vol. 11, no. 2002, pp. 479–517, 2002, doi: 10.1017/S0962492902000077.

[22] R. Mittal, H. Dong, M. Bozkurttas, F. M. Najjar, A. Vargas, and A. von Loebbecke, "A versatile sharp interface immersed boundary method for incompressible flows with complex

boundaries," *J Comput Phys*, vol. 227, no. 10, pp. 4825–4852, May 2008, doi: 10.1016/j.jcp.2008.01.028.

[23] V. Ramanuj, R. Sankaran, and B. Radhakrishnan, "A sharp interface model for deterministic simulation of dendrite growth," *Comput Mater Sci*, vol. 169, Nov. 2019, doi: 10.1016/j.commatsci.2019.109097.

[24] S. Brahmachary, G. Natarajan, V. Kulkarni, and N. Sahoo, "A sharp-interface immersed boundary framework for simulations of high-speed inviscid compressible flows," *Int J Numer Methods Fluids*, vol. 86, no. 12, pp. 770–791, Apr. 2018, doi: 10.1002/FLD.4479.

[25] F. R. Foulkes, *Physical chemistry for engineering and applied sciences*. CRC Press, 2012.

[26] The Engineering ToolBox, "Resistivity and Conductivity - Temperature Coefficients Common Materials," Available at: https://www.engineeringtoolbox.com/resistivity-conductivity-d_418.html.

[27] D. McEligot, W. Swank, D. Cottle, and F. Valentin, "Thermal properties of G-348 graphite," 2016, Accessed: Mar. 13, 2025. [Online]. Available: https://www.osti.gov/biblio/1330693

[28] Inc. Entegris, "Graphite Properties and Characteristics For industrial applications," 2020.

[29] K. Schladitz, S. Peters, D. Reinel-Bitzer, A. Wiegmann, and J. Ohser, "Design of acoustic trim based on geometric modeling and flow simulation for non-woven," *Comput Mater Sci*, vol. 38, no. 1, pp. 56–66, Nov. 2006, doi: 10.1016/J.COMMATSCI.2006.01.018.

[30] A. G. Yiotis, M. E. Kainourgiakis, G. C. Charalambopoulou, and A. K. Stubos, "Microscale characterisation of stochastically reconstructed carbon fiber-based Gas Diffusion Layers; effects of anisotropy and resin content," *J Power Sources*, vol. 320, pp. 153–167, 2016.

Declaration of interests

☒The authors declare that they have no known competing financial interests or personal relationships that could have appeared to influence the work reported in this paper.

☐The authors declare the following financial interests/personal relationships which may be considered as potential competing interests: